

ARTICLE

Open Access

# Evidence for moiré intralayer excitons in twisted $WSe_2/WSe_2$ homobilayer superlattices

Biao Wu<sup>1,2</sup>, Haihong Zheng<sup>1,2</sup>, Shaofei Li<sup>1</sup>, Junnan Ding<sup>1</sup>, Jun He<sup>1</sup>, Yujia Zeng<sup>3</sup>, Keqiu Chen<sup>3</sup>, Zongwen Liu<sup>4,5</sup>, Shula Chen<sup>6</sup>, Anlian Pan<sup>6</sup>✉ and Yanping Liu<sup>1,2,7</sup>✉

## Abstract

Recent advances in twisted van der Waals heterostructure superlattices have emerged as a powerful and attractive platform for exploring novel condensed matter physics due to the interplay between the moiré potential and Coulomb interactions. The moiré superlattices act as a periodic confinement potential in space to capture interlayer excitons (IXs), resulting in moiré exciton arrays, which provide opportunities for quantum emitters and many-body physics. The observation of moiré IXs in twisted transition-metal dichalcogenide (TMD) heterostructures has recently been widely reported. However, the capture and study of the moiré intralayer excitons based on TMD twisted homobilayer (T-HB) remain elusive. Here, we report the observation of moiré intralayer excitons in a  $WSe_2/WSe_2$  T-HB with a small twist angle by measuring PL spectrum. The multiple split peaks with an energy range of 1.55–1.73 eV are different from that of the monolayer  $WSe_2$  exciton peaks. The split peaks were caused by the trapping of intralayer excitons via the moiré potential. The confinement effect of the moiré potential on the moiré intralayer excitons was further demonstrated by the changing of temperature, laser power, and valley polarization. Our findings provide a new avenue for exploring new correlated quantum phenomena and their applications.

## Introduction

Two-dimensional (2D) moiré superlattices are opening up new opportunities for exploring novel correlated physics fundamentals, since almost flat electron bands can be designed to enhance the influence of electron-electron correlation<sup>1–5</sup>. This phenomenon was observed for the first time in graphene-based moiré superlattices, where the graphene moiré systems displayed correlated insulator states, topological phases and unconventional superconductivity<sup>6–8</sup>. Promoted by the graphene-based moiré superlattices, it was predicted that the moiré superlattice based on TMD may have flatter minibands that improve the effect of long-range Coulomb interactions<sup>9–11</sup>.

In contrast to the twisted bilayer graphene, the flat bands only appear at magic angles<sup>12</sup>, while the twisted TMD bilayer has a wider range of angles<sup>10,13</sup>. Therefore, moiré superlattices based on twisted TMD materials can provide a new dimension to explore strongly correlated novel quantum phenomena, such as the quantum emitters and correlated insulators<sup>14–16</sup>.


Moiré superlattices are formed by vertically stacking two monolayers of 2D materials with a small twist angle or lattice mismatch<sup>17</sup>. The moiré potential acts as an ordered array of nanodots in real space by modulating the electronic structure, which essentially modifies the properties of the IXs<sup>18,19</sup>. In addition, the electronic band structure of the moiré superlattice can be designed by the stacking angle, thereby modulating the moiré period and the interaction between the moiré excitons<sup>20,21</sup>. Therefore, moiré superlattices based on TMD offer a powerful platform for quantum electronics and optics<sup>4,5</sup>. Recently, the features of IX trapped in moiré potential have been extensively reported in TMD heterostructure samples<sup>17–20</sup>. The moiré potential acts

Correspondence: Anlian Pan (anlian.pan@hnu.edu.cn) or Yanping Liu (liuyanping@csu.edu.cn)

<sup>1</sup>School of Physics and Electronics, Hunan Key Laboratory for Super-microstructure and Ultrafast Process, Central South University, 932 South Lushan Road, Changsha, Hunan 410083, China

<sup>2</sup>State Key Laboratory of High-Performance Complex Manufacturing, Central South University, 932 South Lushan Road, Changsha, Hunan 410083, China  
Full list of author information is available at the end of the article

© The Author(s) 2022

 **Open Access** This article is licensed under a Creative Commons Attribution 4.0 International License, which permits use, sharing, adaptation, distribution and reproduction in any medium or format, as long as you give appropriate credit to the original author(s) and the source, provide a link to the Creative Commons license, and indicate if changes were made. The images or other third party material in this article are included in the article's Creative Commons license, unless indicated otherwise in a credit line to the material. If material is not included in the article's Creative Commons license and your intended use is not permitted by statutory regulation or exceeds the permitted use, you will need to obtain permission directly from the copyright holder. To view a copy of this license, visit <http://creativecommons.org/licenses/by/4.0/>.

as a periodical trap potential in space to confine the IXs, resulting in moiré exciton arrays<sup>20</sup>. However, reports on moiré intralayer excitons in the TMD T-HB have been absent thus far.

In this work, we report the successful preparation of a WSe<sub>2</sub>/WSe<sub>2</sub> T-HB with an interlayer twist angle approaching zero by the tear-and-stack technique<sup>7,22</sup>. We measured and fitted the second-harmonic generation (SHG) signals of both WSe<sub>2</sub> monolayers at the top and bottom of the sample, and determined that the twist angle between the WSe<sub>2</sub> bilayers was 1.36 ± 0.05. The PL spectrum at 8 K in the T-HB region was fitted by the Lorentzian function to obtain 8 small split peaks that are different from exciton peaks of the monolayer WSe<sub>2</sub>. The energy range of the split peaks was 1.55–1.73 eV, which was attributed to the flat minibands produced by the moiré potential modulation on the electronic structure. In addition, we were able to control the moiré intralayer excitons through the variation of temperature, laser power, and valley polarization, thus achieving the confining effect of the moiré potential on the moiré intralayer excitons. Our results provide a promising opportunity for further exploring new condensed matter physics and its applications.

## Results

The schematic diagram of the moiré superlattice formed by the WSe<sub>2</sub>/WSe<sub>2</sub> T-HB with a small twist angle  $\theta$  is shown in Fig. 1a. The period of the moiré superlattice is  $a_M = a/(2 \sin[\theta/2])$ , where  $a$  is the lattice constant of the WSe<sub>2</sub> monolayer. Figure 1b presents a schematic of the spatial periodic moiré potential generated by the moiré superlattice in Fig. 1a. The in-plane momentum of the system is defined as the high energy level of the moiré potential. The center-of-mass motion of excitons in the moiré potential can be expressed by an effective Hamiltonian<sup>19</sup>

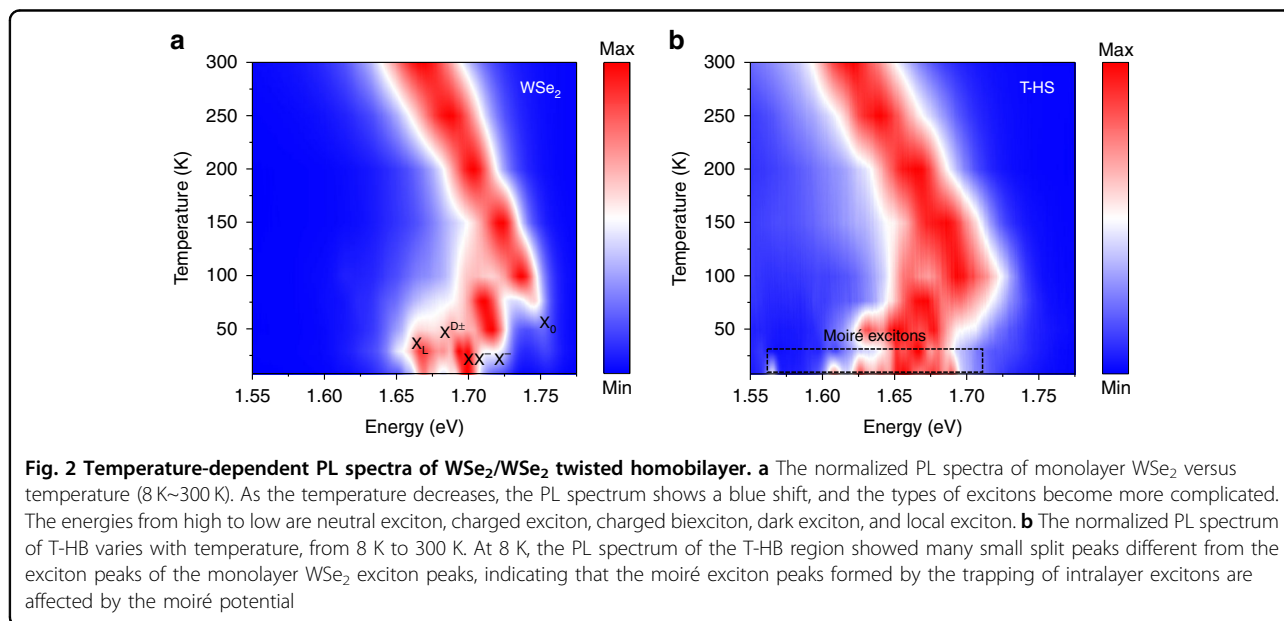
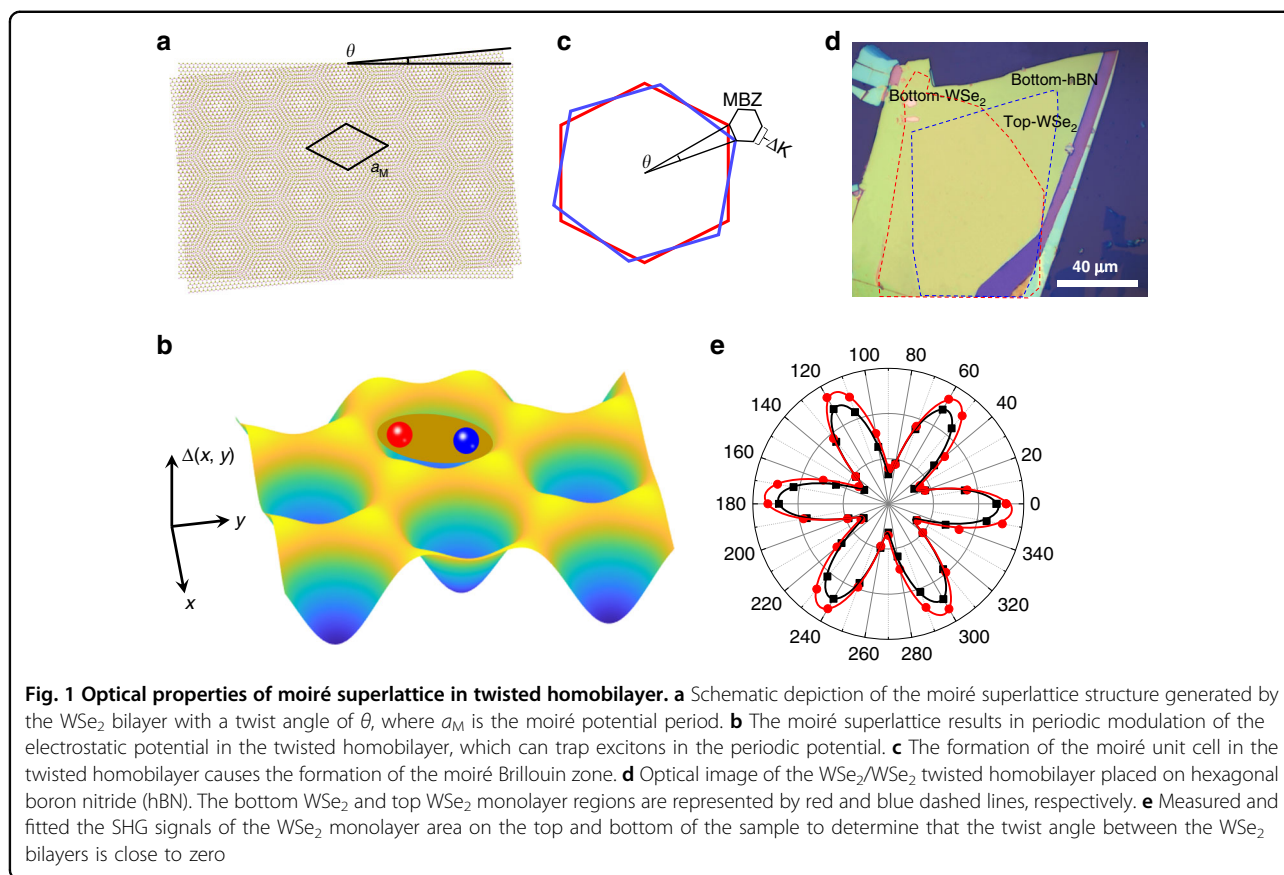
$$H = -\hbar\Omega_0 + \frac{\hbar^2 k^2}{2M} + \Delta(r) \quad (1)$$

where  $\hbar\Omega_0$  is the energy constant of the lowest exciton state energy,  $M$  represents the effective mass of exciton,  $\hbar^2 k^2/(2M)$  is the kinetic energy, and  $\Delta(r)$  is the moiré potential energy. The spatial periodic potential,  $\Delta(r) = \Delta(x, y)$ , can modulate the undisturbed electron band of the monolayer, forming many flat electron minibands, thereby changing the energy band structure of the twisted bilayer. As a consequence, depending on the moiré potential, electrons or holes, and light-excited quasi-particles, such as excitons and exciton complexes may be trapped in the potential. Figure 1c shows the mini-Brillouin zone formed in the WSe<sub>2</sub> bilayer with a rotation angle of  $\theta$ . The size of the Brillouin zone determines the number of moiré cells occupied and the intensity of the optical transition dipole. Figure 1d illustrates the optical image of the sample with the WSe<sub>2</sub>/WSe<sub>2</sub> T-HB, in which the red and blue dashed

areas represent the bottom and top monolayers, respectively. The samples were fabricated following a mechanical exfoliation and tear-and-stack technique. The polarization-dependent SHG signals were measured to determine the twist angle between layers. As shown in Fig. 1e, the fitted data indicate that the interlayer twist angle of the T-HB is close to zero ( $1.36 \pm 0.05^\circ$ ).

To better understand the PL characteristics of the T-HB, we studied the normalized PL spectra of the monolayer and the T-HB region as a function of temperature. Figure 2a shows the PL spectrum of the WSe<sub>2</sub> monolayer with temperature, varying from 8 to 300 K. At 300 K, there is only one peak in the PL spectrum of the WSe<sub>2</sub> monolayer, and its energy is 1.669 eV. As the temperature decreases, the emission peak exhibits a blue shift, which is consistent with the Varshni equation describing the change of the bandgap of various semiconductors with temperature<sup>23</sup>. In addition, it can be clearly observed that the spectral intensity of the monolayer WSe<sub>2</sub> shifts neutral exciton ( $X_0$ ) to charged exciton ( $X^-$ ), and then to charged biexcitons ( $XX^-$ ), which is caused by the reduction of electron thermal fluctuations<sup>24,25</sup>. At 8 K, there are abundant excitons in the PL spectrum, and the energies from high to low are  $X_0$ ,  $X^-$ ,  $XX^-$ , dark exciton ( $X^{D+}$ ) and local exciton ( $X_L$ ), which can be identified by PL spectrum<sup>26,27</sup>. Figure 2b presents the results of the temperature-dependent PL for the T-HB. As the temperature cools, the emission peak appears blue shift. Noticeably, when the temperature is 8 K, the PL spectra show many small splitting peaks different from the WSe<sub>2</sub> monolayer exciton peaks, which is caused by the moiré potential in the T-HB.

To further explore the optical properties of the T-HB, we compared the PL spectra of the monolayer and the T-HB region at 8 K as shown in Fig. 3a. It can be clearly observed that the PL spectrum of the T-HB region shows two distinct IX peaks in the low energy range. The appearance of IX peaks indicates that the two monolayers of WSe<sub>2</sub> were coupled very well. Interestingly, the multiple split peaks at 1.55–1.73 eV are different from the monolayer WSe<sub>2</sub> exciton peaks, indicating the presence of moiré superlattices in our sample, which is caused by the trapping of intralayer excitons by the moiré potential<sup>19,28</sup>. For the WSe<sub>2</sub>/WSe<sub>2</sub> T-HB with a small twist angle, the optical transition of excitons is significantly different from the WSe<sub>2</sub> monolayer, due to the formation of the moiré Brillouin zone that causes the formation of flat minibands in T-HB. Figure 3b shows the PL spectra of homobilayers with twist angles of 1.36° and 3°, with 8 and 12 small peaks obtained by Lorentzian function fitting, respectively. For the WSe<sub>2</sub>/WSe<sub>2</sub> homobilayer with a twist angle of 1.36°, the central emission energies extracted from the fitted eight small splitting peaks for the homobilayer with a twist angle of 1.36° are 1.593, 1.621, 1.638, 1.653, 1.672, 1.686, 1.694, and 1.702 eV. The moiré potential depths of the 1.36° and 3° twisted homobilayers in our



experiments are 109 and 215 meV, respectively, which are similar to the results previously reported by Tran et al.<sup>19</sup> As the twist angle increases, the moiré superlattice period decreases. The moiré potential is inversely proportional to

the moiré superlattice period, so the moiré potential increases with the twist angle. The experimental results show that the homobilayer with a larger twist angle has more splitting and broader energy peaks, which is consistent

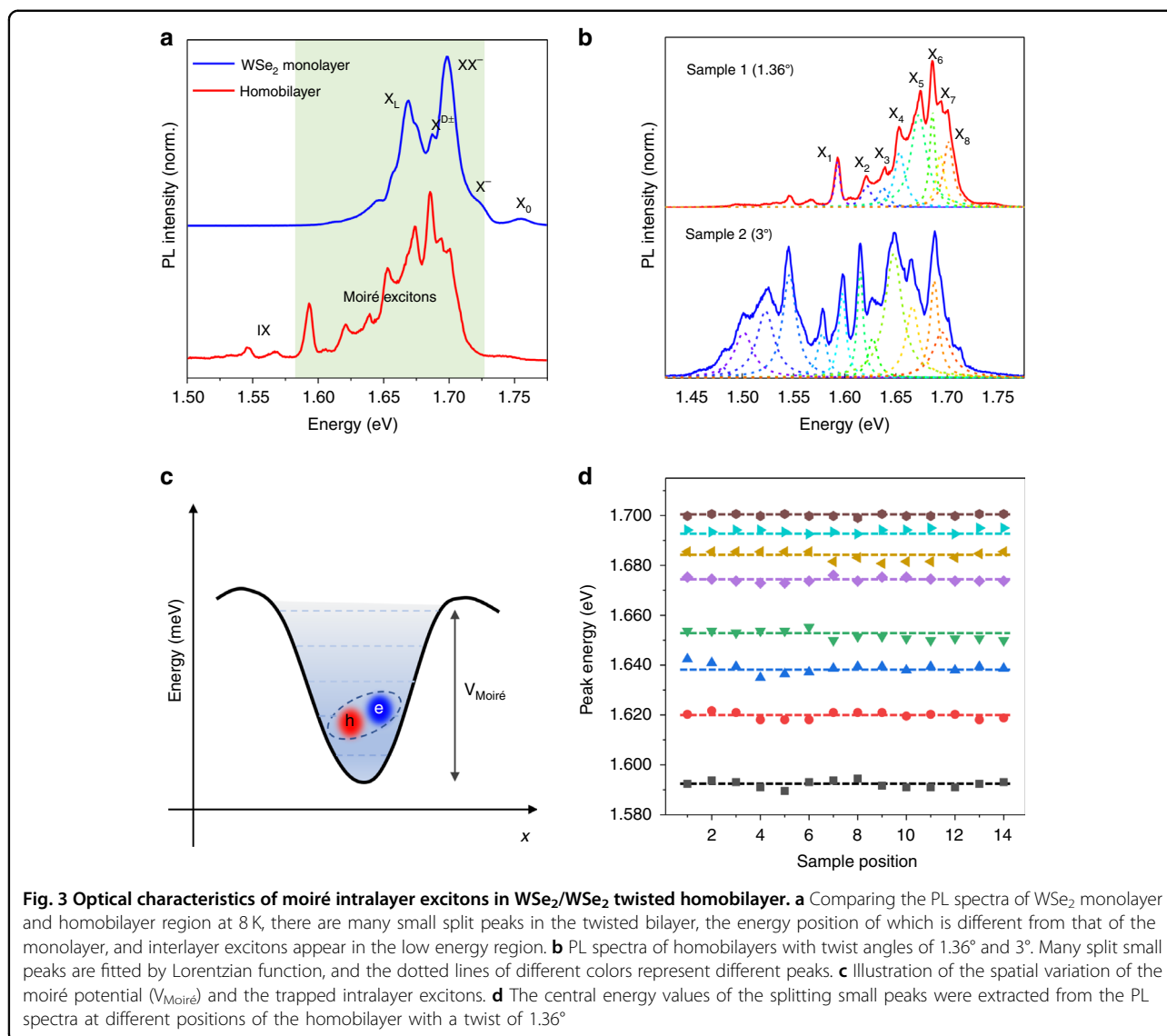
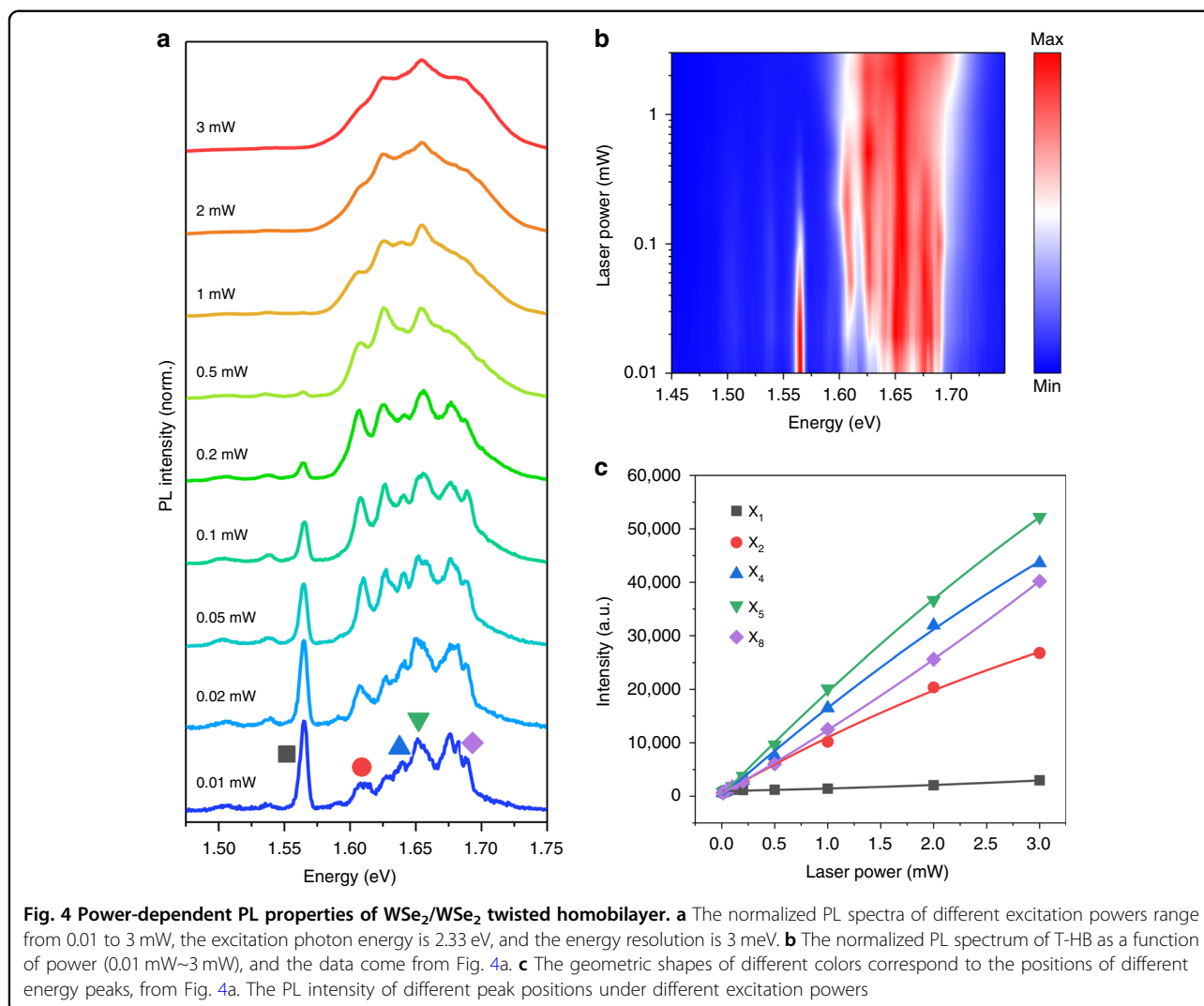


**Fig. 3 Optical characteristics of moiré intralayer excitons in WSe<sub>2</sub>/WSe<sub>2</sub> twisted homobilayer.** **a** Comparing the PL spectra of WSe<sub>2</sub> monolayer and homobilayer region at 8 K, there are many small split peaks in the twisted bilayer, the energy position of which is different from that of the monolayer, and interlayer excitons appear in the low energy region. **b** PL spectra of homobilayers with twist angles of 1.36° and 3°. Many split small peaks are fitted by Lorentzian function, and the dotted lines of different colors represent different peaks. **c** Illustration of the spatial variation of the moiré potential ( $V_{\text{Moiré}}$ ) and the trapped intralayer excitons. **d** The central energy values of the splitting small peaks were extracted from the PL spectra at different positions of the homobilayer with a twist of 1.36°

with the theoretical results<sup>29</sup>. Figure 3c depicts a schematic diagram of the spatial variation of the moiré potential and the trapping of intralayer excitons. The formation of the moiré Brillouin zone in Fig. 1c changes the electronic structure in the T-HB, resulting in many flat minibands, which are marked in the moiré potential with dashed lines. In WSe<sub>2</sub>/WSe<sub>2</sub> T-HB with a small twist angle, the Bohr radius of excitons is larger than the lattice constant of monolayer WSe<sub>2</sub>, but smaller than the moiré period<sup>19</sup>. Therefore, the intralayer excitons can be regarded as particles moving slowly in the moiré potential, which appear as small split peaks on the PL spectrum. Figure 3d shows the central energies of eight small split peaks extracted from the PL spectra at different positions in the T-HB region, indicating that the PL spectra can be repeated at different positions in the T-HB.

To obtain more detailed information about the moiré potential, we investigated the power-dependent PL spectrum in the T-HB region at 8 K. Figure 4a depicts the PL spectra at different excitation powers from 0.01 to 3 mW at an excitation wavelength of 532 nm. Under the low excitation power (<0.2 mW), the shape of the PL spectrum remains basically unchanged, and each small split emission peak in PL spectrum can be clearly observed. With the increase of the power, the flat minibands in the moiré potential are gradually filled by trapping excitons and finally reach saturation, which appears as a decrease in exciton peaks and an increase in peak width on the PL spectrum. The results show that as the power increases, the modulation of the intralayer excitons is weakened by the moiré potential<sup>20</sup>. Figure 4b presents the normalized PL spectrum as a function of



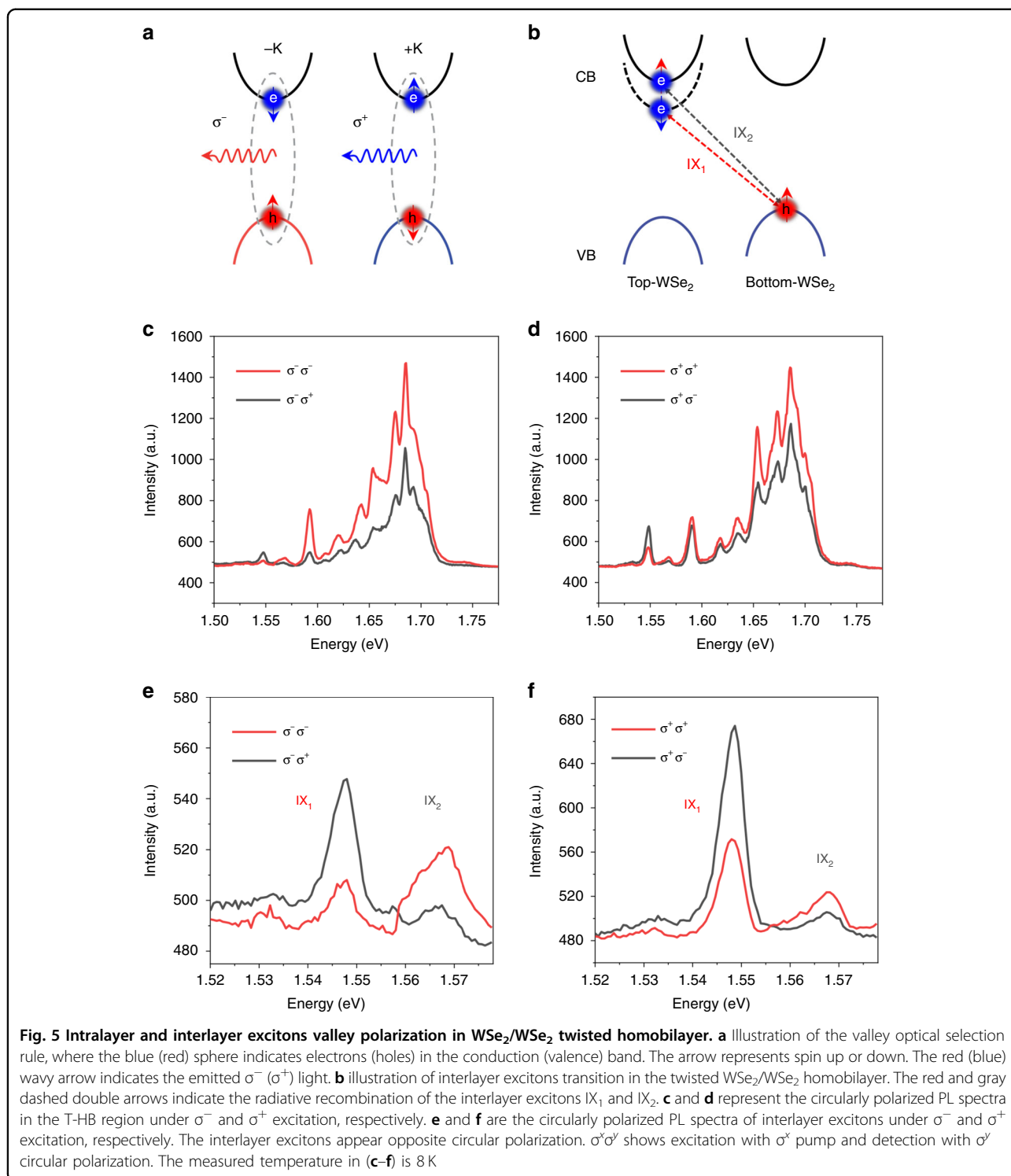
power, from 0.01 to 3 mW. The color plot, using data from Fig. 4a, makes it more intuitive to observe the evolution of excitons with power. It can be clearly seen that as the power increases, the  $X_1$  energy level is gradually filled and finally reaches saturation, and the moiré excitons change from multiple small split peaks to the main peak dominated by intralayer excitons. The results show that there are many small split peaks in the PL spectrum at low power, indicating that there is a confinement potential for trapping intralayer excitons, caused by the flat minibands in the moiré Brillouin zone. Figure 4c quantitatively studied the PL intensity of some peaks extracted from the PL spectrum as a function of power. The shapes of different colors indicate the different peak positions which are derived from Fig. 4a. It can be observed that the  $X_1$  exciton level at low power is quickly filled to reach saturation ( $>0.1$  mW). Notably, when the power is  $>1$  mW, the PL intensity of the  $X_1$  peak appears to be enhanced, which is due to the

influence of the PL spectra of interlayer excitons and moiré excitons with similar energies. As the power increases, the flat minibands of higher energy levels are sequentially filled and gradually reach saturation. Exciton filling is sequentially from low energy level to high energy level. While  $X_8$  is at the highest energy level, and there is no sign of saturation at 3 mW, so the  $X_8$  peak continues to grow rapidly with the increase of power, which is consistent with previous report<sup>20</sup>. The results show that the relaxation and transfer of moiré excitons from higher energy levels to lower energy levels are effective at low power, and the moiré potential gradually loses its modulation effect of intralayer excitons as the power increases.

## Discussion

To better understand the circular polarization properties of moiré intralayer excitons, we studied the polarization-resolved PL spectrum of T-HB at 8 K.





According to the optical selection rule shown in Fig. 5a, the valley is coupled to the PL circularly. Hence, the characteristic of the valley can be characterized by the circular polarization-resolved PL measurement. When excited with  $\sigma^-$  (or  $\sigma^+$ ) pump light, the co- ( $\sigma^-$  detection) and cross- ( $\sigma^+$  detection) circularly polarized PL spectra

were collected<sup>30</sup>. Here we define circular polarization as<sup>31</sup>

$$P_{\sigma^-} = [I(\sigma^-)] - I(\sigma^+) / [I(\sigma^-) + I(\sigma^+)] \quad (2)$$

where  $I(\sigma^\pm)$  represents the measured PL intensity. Figure 5b shows the IX transitions of the type-II structure. Due to the

spin-orbit coupling effect<sup>32</sup>, the conduction band of WSe<sub>2</sub> splits into spin-up and spin-down energy levels, where electrons in these two energy levels combine with holes in the adjacent layer valence band to form interlayer excitons IX<sub>1</sub> and IX<sub>2</sub>. Figure 5c shows that when excited with  $\sigma^-$  pump light, the emission intensity detected with  $\sigma^-$  is stronger than that detected with  $\sigma^+$  when the energy is in the range of 1.55–1.73 eV. Similarly, Fig. 5d presents that the emission intensity detected with  $\sigma^+$  is stronger than that detected with  $\sigma^-$  when excited with  $\sigma^+$  pump light. The difference in emission intensity detected by  $\sigma^+$  and  $\sigma^-$  is caused by the valley optical selection rule<sup>33–35</sup>. Under the excitation of  $\sigma^-$  pump light, carriers are generated in the  $-K$  valley and recombined to emit  $\sigma^-$  light, while no carriers are generated in the  $+K$  valley. However, the emission light is detected by  $\sigma^+$  due to intervalley scattering. Meanwhile, only carriers in the  $+K$  valley are excited when excited by  $\sigma^+$  pump light.

Figure 5e, f shows that the PL spectra of the T-HB region at 8 K appear with two distinct emission peaks around 1.55 eV, consistent with the energy range of the interlayer exciton peaks<sup>36–40</sup>. Meanwhile, the energy difference between the two IX peaks is 20 meV, which is also in good agreement with previous reports<sup>38,41</sup>. The IX peak splitting phenomenon is attributed to the spin-orbit coupling effect of the conduction band of WSe<sub>2</sub><sup>32,38</sup>. The WSe<sub>2</sub>/WSe<sub>2</sub> T-HB forms a type-II band alignment, and Fig. 5b shows the IX transition of the type-II structure. Because of the spin-orbit coupling effect, the conduction band of WSe<sub>2</sub> is split into spin-up and spin-down energy levels, and electrons in these two energy levels combine with holes in the valence band of adjacent layers to form interlayer excitations IX<sub>1</sub> and IX<sub>2</sub> due to forceful Coulomb interactions<sup>38,40</sup>. The lifetime of these IXs is much longer than that of direct excitons, which is critical for long-lived exciton devices<sup>42–44</sup>. Interestingly, under the excitation of circularly polarized light, it can be clearly observed that both IX<sub>1</sub> and IX<sub>2</sub> exhibit cross-polarization<sup>31</sup>. The results indicate that the spin directions of the conduction band and valence band energy levels of the interlayer excitons IX<sub>1</sub> are opposite, while the spin directions of the energy levels of the interlayer excitons IX<sub>2</sub> are the same opposite as shown in Fig. 5b.

We have prepared a high-quality WSe<sub>2</sub>/WSe<sub>2</sub> HB with a small twist angle, and successfully observed moiré intralayer excitons at 8 K by measuring the PL spectrum. The multiple split peaks with energies ranging from 1.55 to 1.73 eV are different from that of the monolayer WSe<sub>2</sub> exciton peaks, which were caused through the trapping of intralayer excitons by the moiré potential. In addition, two distinct IX peaks appear at about 1.55 eV, with an energy difference of 20 meV, which is caused by the spin-orbit coupling effect. Furthermore, the effects of changes in temperature and laser

power, as well as the valley polarization on the moiré excitons were performed and the key observed spectral features were explained. Our results provide new opportunities for quantum emitters and many-body phenomena.

## Materials and methods

### Sample fabrication

Monolayer WSe<sub>2</sub> and hBN flakes were obtained from bulk crystals (HQ graphene) by mechanical exfoliation. The T-HB samples were prepared under the microscope using the tear-and-stack technique<sup>7,22</sup>. The sample preparation process (including mechanical exfoliation, tearing, and stacking) was performed in a glove box transfer platform under a fully enclosed nitrogen atmosphere with water content below 0.02 ppm and an oxygen content below 0.2 ppm. A glass slide covered with a piece of polydimethylsiloxane (PDMS) and a drop of polycarbonate (PC) was used first to pick up a part of the monolayer WSe<sub>2</sub>, followed by twisting the remaining part of the monolayer WSe<sub>2</sub> at a small angle, and then stack the picked-up first part of the monolayer WSe<sub>2</sub> vertically on to the remaining monolayer WSe<sub>2</sub>, and then pick it up together. The next step is to transfer the WSe<sub>2</sub> bilayer onto the hBN sheet and peel off the PC glue. The PC glue was dissolved in dichloromethane at room temperature for 2 h. Finally, the prepared samples were annealed in an argon atmosphere at 300 °C for 3 h to make the sample interface cleaner. There were no visible cracks, wrinkles, or contamination in the optical image, indicating that we successfully prepared high-quality T-HB samples. It should be mentioned that the sample preparation may confine water vapor at the interface, but the proportion of water vapor in the total area is negligible compared to the area of the T-HB region.

### Optical measurements

All-optical data were measured on the WITec Alpha 300R system, which has 50× objective lenses and a light spot of nearly 1  $\mu\text{m}$ . Before the optical measurement, the pressure in the cryogenic chamber should be kept below  $10^{-5}$  Pa, and then the chamber was heated to 350 K for 20 min to remove the water vapor. Finally, optical measurements were performed on the WITec Alpha 300R Raman system when the sample temperature reached 8 K. The model number of the cryogenic refrigeration system is C04-005-044 from Cryo Industries of America. The excitation light source of the SHG signal was a 1064 nm pulsed laser, and the excitation wavelength of the excitation light source measured by other data was 532 nm (2.33 eV). The angle data shown in Fig. 1e is fitted by a sine function,  $y = y_0 + A \sin(B\alpha + \varphi)$ , where  $y$  is the intensity of SHG,  $y_0$ ,  $A$ ,  $B$  are constants,  $\alpha$  is the angle of rotation of the half-wave plate, and  $\varphi$  is a fitting parameter defining the relative orientation of TMD crystal lattices. The twist angle between the two monolayers can be deduced by fitting the resulting function.

### Acknowledgements

The authors acknowledge support from the National Natural Science Foundation of China (Grant No. 61775241), Hunan province key research and development project (Grant No. 2019GK2233), Hunan Provincial Science Fund for Distinguished Young Scholars (Grant No. 2020JJ2059), and the Youth Innovation Team (Grant No. 2019012) of CSU, the Science and Technology Innovation Basic Research Project of Shenzhen (Grant No. JCYJ20190806144418859), the National Natural Science Foundation of China (Nos. 62090035 and U19A2090); the Key Program of Science and Technology Department of Hunan Province (2019XK2001, 2020XK2001). The authors are also thankful for the support of the High-Performance Complex Manufacturing Key State Lab Project, Central South University (Grant No. ZZYJKT2020-12). Z.W.L. thanks the support from the Australian Research Council (ARC Discovery Project, DP180102976).

### Author details

<sup>1</sup>School of Physics and Electronics, Hunan Key Laboratory for Super-microstructure and Ultrafast Process, Central South University, 932 South Lushan Road, Changsha, Hunan 410083, China. <sup>2</sup>State Key Laboratory of High-Performance Complex Manufacturing, Central South University, 932 South Lushan Road, Changsha, Hunan 410083, China. <sup>3</sup>Department of Applied Physics, School of Physics and Electronics, Hunan University, Changsha 410082, China. <sup>4</sup>School of Chemical and Biomolecular Engineering, The University of Sydney, Sydney, NSW 2006, Australia. <sup>5</sup>The University of Sydney Nano Institute, The University of Sydney, Sydney, NSW 2006, Australia. <sup>6</sup>Hunan Institute of Optoelectronic Integration, College of Materials Science and Engineering, Hunan University, Changsha, Hunan 410082, China. <sup>7</sup>Shenzhen Research Institute of Central South University, A510a, Virtual University Building, Southern District, High-tech Industrial Park, Yuehai Street, Nanshan District, Shenzhen, China

### Author contributions

Y.P.L. designed and managed the project. B.W. fabricated the device and performed the Raman and PL characterizations. B.W., S.F.L., and Z.Y.L. performed the low-temperature measurements. Y.P.L., B.W., J.H., A.L.P., J.N.D., K.Q.C., S.L.C., Z.W.L., and Y.J.Z. provided a vital interpretation of the data. Y.P.L., B.W., and Z.W.L. drafted the paper. All authors read and contributed to the revising of the manuscript.

### Conflict of interest

The authors declare no competing interests.

Received: 7 December 2021 Revised: 27 April 2022 Accepted: 15 May 2022  
Published online: 01 June 2022

### References

- Nuckolls, K. P. et al. Strongly correlated Chern insulators in magic-angle twisted bilayer graphene. *Nature* **588**, 610–615 (2020).
- Yu, H. Y. et al. Moiré excitons: from programmable quantum emitter arrays to spin-orbit-coupled artificial lattices. *Sci. Adv.* **3**, e1701696 (2017).
- Ghiotto, A. et al. Quantum criticality in twisted transition metal dichalcogenides. *Nature* **597**, 345–349 (2021).
- Liu, Y. P. et al. Moiré superlattices and related moiré excitons in twisted van der Waals heterostructures. *Chem. Soc. Rev.* **50**, 6401–6422 (2021).
- Kennes, D. M. et al. Moiré heterostructures as a condensed-matter quantum simulator. *Nat. Phys.* **17**, 155–163 (2021).
- Cao, Y. et al. Correlated insulator behaviour at half-filling in magic-angle graphene superlattices. *Nature* **556**, 80–84 (2018).
- Cao, Y. et al. Unconventional superconductivity in magic-angle graphene superlattices. *Nature* **556**, 43–50 (2018).
- Yankowitz, M. et al. Tuning superconductivity in twisted bilayer graphene. *Science* **363**, 1059–1064 (2019).
- Li, H. Y. et al. Imaging moiré flat bands in three-dimensional reconstructed  $WSe_2/WSe_2$  superlattices. *Nat. Mater.* **20**, 945–950 (2021).
- Naik, M. H. & Jain, M. Ultraflat bands and shear solitons in moiré patterns of twisted bilayer transition metal dichalcogenides. *Phys. Rev. Lett.* **121**, 266401 (2018).
- Wu, F. C. et al. Hubbard model physics in transition metal dichalcogenide moiré bands. *Phys. Rev. Lett.* **121**, 026402 (2018).
- Tilak, N. et al. Flat band carrier confinement in magic-angle twisted bilayer graphene. *Nat. Commun.* **12**, 4180 (2021).
- Naik, M. H. et al. Origin and evolution of ultraflat bands in twisted bilayer transition metal dichalcogenides: realization of triangular quantum dots. *Phys. Rev. B* **102**, 075413 (2020).
- Shimazaki, Y. et al. Strongly correlated electrons and hybrid excitons in a moiré heterostructure. *Nature* **580**, 472–477 (2020).
- Tang, Y. H. et al. Simulation of Hubbard model physics in  $WSe_2/WSe_2$  moiré superlattices. *Nature* **579**, 353–358 (2020).
- Seyler, K. L. et al. Signatures of moiré-trapped valley excitons in  $MoSe_2/WSe_2$  heterobilayers. *Nature* **567**, 66–70 (2019).
- Liu, E. R. et al. Signatures of moiré trions in  $WSe_2/MoSe_2$  heterobilayers. *Nature* **594**, 46–50 (2021).
- Wang, X. et al. Moiré trions in  $MoSe_2/WSe_2$  heterobilayers. *Nat. Nanotechnol.* **16**, 1208–1213 (2021).
- Tran, K. et al. Evidence for moiré excitons in van der Waals heterostructures. *Nature* **567**, 71–75 (2019).
- Shinokita, K. et al. Resonant coupling of a moiré exciton to a phonon in a  $WSe_2/MoSe_2$  heterobilayer. *Nano Lett.* **21**, 5938–5944 (2021).
- Li, Z. D. et al. Interlayer exciton transport in  $MoSe_2/WSe_2$  heterostructures. *ACS Nano* **15**, 1539–1547 (2021).
- Kim, K. et al. Van der Waals heterostructures with high accuracy rotational alignment. *Nano Lett.* **16**, 1989–1995 (2016).
- Li, C. C. et al. Temperature dependent energy gap shifts of single color center in diamond based on modified Varshni equation. *Diam. Relat. Mater.* **74**, 119–124 (2017).
- Ross, J. S. et al. Electrical control of neutral and charged excitons in a monolayer semiconductor. *Nat. Commun.* **4**, 1474 (2013).
- Wu, B. et al. Observation of double indirect interlayer exciton in  $MoSe_2/WSe_2$  heterostructure. *Nano Res.* **15**, 2661–2666 (2022).
- Jones, A. M. et al. Optical generation of excitonic valley coherence in monolayer  $WSe_2$ . *Nat. Nanotechnol.* **8**, 634–638 (2013).
- Yu, J. et al. Observation of double indirect interlayer exciton in  $WSe_2/WSe_2$  heterostructure. *Opt. Express* **28**, 13260–13268 (2020).
- Marcellina, E. et al. Evidence for moiré trions in twisted  $MoSe_2$  homobilayers. *Nano Lett.* **21**, 4461–4468 (2021).
- Wu, F. C., Lovorn, T. & MacDonald, A. H. Theory of optical absorption by interlayer excitons in transition metal dichalcogenide heterobilayers. *Phys. Rev. B* **97**, 035306 (2018).
- Tan, Q. H. et al. Layer-engineered interlayer excitons. *Sci. Adv.* **7**, eabh0863 (2021).
- Hanbicki, A. T. et al. Double indirect interlayer exciton in a  $MoSe_2/WSe_2$  van der Waals heterostructure. *ACS Nano* **12**, 4719–4726 (2018).
- Rivera, P. et al. Observation of long-lived interlayer excitons in monolayer  $MoSe_2-WSe_2$  heterostructures. *Nat. Commun.* **6**, 6242 (2015).
- Mak, K. F. et al. Control of valley polarization in monolayer  $MoS_2$  by optical helicity. *Nat. Nanotechnol.* **7**, 494–498 (2012).
- Cao, T. et al. Valley-selective circular dichroism of monolayer molybdenum disulphide. *Nat. Commun.* **3**, 887 (2012).
- Cao, L. K. et al. Valley-polarized local excitons in  $WSe_2/WSe_2$  vertical heterostructures. *Opt. Express* **28**, 22135–22143 (2020).
- Scuri, G. et al. Electrically tunable valley dynamics in twisted  $WSe_2/WSe_2$  bilayers. *Phys. Rev. Lett.* **124**, 217403 (2020).
- Lindlau, J. et al. The role of momentum-dark excitons in the elementary optical response of bilayer  $WSe_2$ . *Nat. Commun.* **9**, 2586 (2018).
- Sun, Z. et al. Observation of the interlayer exciton gases in  $WSe_2$ -p- $WSe_2$  heterostructures. *ACS Photonics* **7**, 1622–1627 (2020).
- Zeng, C. et al. Observation of split defect-bound excitons in twisted  $WSe_2/WSe_2$  homostructure. *Appl. Phys. Lett.* **117**, 153103 (2020).
- Wang, Z. F. et al. Electrical tuning of interlayer exciton gases in  $WSe_2$  bilayers. *Nano Lett.* **18**, 137–143 (2018).
- Kośmider, K., González, J. W. & Fernández-Rossier, J. Large spin splitting in the conduction band of transition metal dichalcogenide monolayers. *Phys. Rev. B* **88**, 245436 (2013).
- Miller, B. et al. Long-lived direct and indirect interlayer excitons in van der Waals heterostructures. *Nano Lett.* **17**, 5229–5237 (2017).
- Unuchek, D. et al. Room-temperature electrical control of exciton flux in a van der Waals heterostructure. *Nature* **560**, 340–344 (2018).
- Calman, E. V. et al. Indirect excitons and trions in  $MoSe_2/WSe_2$  van der Waals heterostructures. *Nano Lett.* **20**, 1869–1875 (2020).